
Conditioning Protein Generation via Hopfield Pattern Multiplicity

Jeffrey D. Varner

R.F. Smith School of Chemical and Biomolecular Engineering
Cornell University, Ithaca, NY 14850
jdv27@cornell.edu

Abstract

Protein sequence generation via stochastic attention produces plausible family members from small alignments without training, but treats all stored sequences equally and cannot direct generation toward a functional subset of interest. We show that a single scalar parameter, added as a bias to the sampler’s attention logits, continuously shifts generation from the full family toward a user-specified subset, with no retraining and no change to the model architecture. A practitioner supplies a small set of sequences (for example, hits from a binding screen) and a multiplicity ratio that controls how strongly generation favors them. The method is agnostic to what the subset represents: binding, stability, specificity, or any other property. We find that the conditioning is exact at the level of the sampler’s internal representation, but that the decoded sequence phenotype can fall short because the dimensionality reduction used to encode sequences does not always preserve the residue-level variation that defines the functional split. We term this discrepancy the calibration gap and show that it is predicted by a simple geometric measure of how well the encoding separates the functional subset from the rest of the family. Experiments on five Pfam families (Kunitz, SH3, WW, Homeobox, and Forkhead domains) confirm the monotonic relationship between separation and gap across a fourfold range of geometries. Applied to omega-conotoxin peptides targeting a calcium channel involved in pain signaling, curated seeding from 23 characterized binders produces over a thousand candidates that preserve the primary pharmacophore and all experimentally identified binding determinants. These results show that stochastic attention enables practitioners to expand a handful of experimentally characterized sequences into diverse candidate libraries without retraining a generative model.

1 Introduction

Generating novel protein sequences that fold correctly and perform a desired function is a central goal of computational protein engineering. Several classes of methods now address this problem. Deep generative models, including variational autoencoders [1], autoregressive language models [2], and diffusion models [3], learn sequence distributions from large databases and can produce diverse candidates, but require substantial training data and GPU resources. Structure-conditioned inverse folding methods [4] design sequences for a given backbone but require a target structure as input. Protein language models [5] trained on evolutionary databases can score or sample sequences, but conditioning them on a specific functional property typically requires fine-tuning on labeled data. Profile HMMs [6] capture family-level statistics from alignments but, as we show below, produce sequences with low structural confidence and poor compositional fidelity. For the scarce-data regime (families with tens to hundreds of members, typical of Pfam seed alignments), most learned models lack sufficient training signal.

Stochastic attention (SA) was developed for this regime [7]. SA treats the energy function of a modern Hopfield network, constructed directly from a small family alignment, as a Boltzmann density and samples from it using Langevin dynamics. The method requires no training, runs on a laptop, and produces sequences that preserve family-level amino acid composition, per-position conservation, and predicted three-dimensional fold. A key limitation, however, is that SA treats all sequences in the alignment equally. Every family member contributes the same weight to the energy landscape, so the sampler explores the full family distribution without preference for any functional subset. In practice, experimentalists often want something more specific: not just “a plausible Kunitz domain,” but a Kunitz domain that *inhibits trypsin*; not just “a plausible SH3 domain,” but one that binds a particular proline-rich motif. Family alignments define a shared fold (all 99 Kunitz sequences share the same disulfide framework and double-loop architecture), but the members differ in which target they bind, and that specificity is encoded in a small number of positions (e.g., the P1 contact residue) rather than in the global fold. The alignment captures structure; the practitioner wants to condition on function. The question is: *how can we condition the generative process on a functional subset without retraining?*

A seemingly simple answer is to *curate* the input, restricting the alignment to only those sequences that a practitioner has identified (through experimental screens, literature annotation, or functional assays) as belonging to the functional subset of interest. SA then generates new sequences in their image. We show that this strategy works: even three designated input sequences suffice for complete phenotype transfer in the Kunitz domain. But hard curation discards all remaining family members, losing the fold-level constraints they provide. A more principled approach would retain the full family while continuously upweighting the designated subset. SA works by encoding each sequence in the alignment as a column in a matrix (the memory matrix), then running a physics-inspired sampler that generates new sequences by taking noisy steps through the landscape defined by these stored sequences. At each step, the sampler computes an attention distribution over the stored sequences and moves toward a weighted average of them. The key observation we exploit is that adding a bias term to these attention scores deepens the energy wells around specific sequences, causing the sampler to spend more time near them. Concretely, we assign a multiplicity weight $r_k > 0$ to each stored sequence and add $\log r_k$ to its attention score before the softmax normalization. A single parameter, the multiplicity ratio $\rho = r_{\text{designated}}/r_{\text{background}}$, controls the strength of this bias: $\rho = 1$ recovers standard SA (no preference), while increasing ρ shifts generation toward the designated subset. No sequences are duplicated, no parameters are trained, and no architectural changes are needed. The method is agnostic to what the designated subset represents (binding, thermostability, organism of origin); it simply biases the sampler toward the sequences the user points to.

In this study, we developed the theory of multiplicity-weighted SA and tested it on five Pfam protein families (Kunitz, SH3, WW, Homeobox, and Forkhead domains) spanning a range of family sizes ($K = 55\text{--}420$) and functional-subset geometries. We showed that the multiplicity weights enter the sampler as a simple logit bias, preserving the analytic score function and $\mathcal{O}(dK)$ cost of the original method. The energy-level conditioning is exact: the softmax attention on designated patterns matches the target fraction to within 0.3% at all multiplicity ratios tested. However, we found that the decoded sequence phenotype can fall short of this target, because the PCA encoding that compresses sequences into the sampler’s state space does not always preserve the residue-level variation that defines the functional split. We termed this discrepancy the calibration gap and showed that it is predicted by a simple geometric quantity, the Fisher separation index S , which measures how well PCA separates designated from background sequences. Across five families spanning a fourfold range of S , the gap decreased monotonically with increasing separation ($R^2 = 0.80$). This provides a practitioner’s decision rule: compute S before generating any sequences; if S is high, multiplicity weighting transfers the phenotype directly; if S is low, use hard curation instead.

2 Results

We evaluated SA on six protein families spanning a range of sizes, functions, and PCA-space geometries (Table 1). Five Pfam seed families (Kunitz domains (PF00014, $K = 99$), SH3 domains (PF00018, $K = 55$), WW domains (PF00397, $K = 420$), Homeobox domains (PF00046, $K = 136$), and Forkhead domains (PF00250, $K = 246$)) were used to benchmark both hard curation and multiplicity-weighted conditioning, with designated subsets defined by known functional-site residues. A sixth family, the ω -conotoxin O-superfamily ($K = 74$, curated from SwissProt), was used

to test hard curation on a therapeutically relevant peptide system targeting the Cav2.2 calcium channel. For each family, we split sequences into designated and background subsets based on an experimentally validated phenotype marker, built conditioned memory matrices, and generated sequences via Langevin dynamics at the entropy-inflection inverse temperature β^* . The Fisher separation index S , a measure of how well PCA separates designated from background sequences, varied from 0.11 (WW, heavily interleaved) to 0.42 (Homeobox, well-separated), providing a natural axis along which to test the limits of multiplicity-weighted conditioning.

Hard curation and the small-set amplifier. We restricted the memory matrix to a user-designated functional subset of Kunitz domains (PF00014; $K = 99$ sequences, $L = 53$ aligned positions) and tested whether subset-specific phenotype transfers to generated sequences (Fig. 1). Kunitz domains are serine protease inhibitors whose binding specificity depends on the P1 residue at the primary contact site with the target protease: Lys or Arg at P1 confers strong trypsin inhibition, while other residues (Gly, Gln, Asn) do not [8]. We designated the 32 sequences with K/R at P1 as the functional subset ($K_{\text{des}} = 32$) and the remaining 67 as background ($K_{\text{bg}} = 67$), built separate memory matrices from each group, found β^* for each via entropy inflection, and generated 930 sequences per condition (30 chains \times 5,000 steps, thinned after burn-in). We observed that 100% of designated-subset-conditioned sequences had K/R at P1; 0% of background-conditioned sequences did; and full-family generation produced 41% K/R, close to the natural proportion ($32/99 = 32\%$), showing that the designated phenotype was fully inherited while the fold-level composition was approximately preserved. Sequence-level inspection showed that the top strong-binder-conditioned sequences preserved all highly conserved positions (11/11), all six cysteines, and carried K/R at P1, while introducing 19-26 substitutions concentrated at variable sites; per-position Shannon entropy tracked the stored MSA closely ($r = 0.988$ for full-family, $r = 0.932$ for strong-conditioned), with the largest deviation at P1 where conditioning collapsed diversity to K/R (Fig. 5). To determine the minimum input size required for reliable transfer, we subsampled $K_{\text{des}} \in \{3, 5, 8, 10, 15, 20, 25, 32\}$ from the Kunitz K/R subset (3 replicates each), built curated memory matrices, and generated sequences. We found that P1 phenotype fidelity was 100% at every sample size, including $K_{\text{des}} = 3$, but that small input sets reduced diversity: pairwise sequence diversity increased from 0.36 ($K_{\text{des}} = 3$) to 0.50 ($K_{\text{des}} = 32$), and KL divergence decreased from 0.047 to 0.009 over the same range, which is consistent with fewer stored patterns constraining the PCA subspace and reducing the volume accessible to the Langevin chain (Fig. 1). These results support the “small-set amplifier” framing: a practitioner with as few as 5–10 experimentally characterized sequences (for instance, hits from a phage display screen) can generate hundreds of candidates that maintain the input phenotype while introducing sequence diversity (pairwise diversity ≥ 0.45 for $K_{\text{des}} \geq 10$).

Multiplicity-weighted conditioning and the calibration gap. We tested multiplicity-weighted generation on the Kunitz family ($K = 99$, $K_{\text{des}} = 32$ strong trypsin binders, $K_{\text{bg}} = 67$ background), sweeping ρ from 1 (standard SA, no bias) to 1,000 (Fig. 2, Table 2). For each ρ , we computed the multiplicity vector \mathbf{r} , found $\beta^*(\mathbf{r})$ via entropy inflection on the weighted attention distribution, and generated 930 sequences (30 chains). Two quantities were tracked at each ρ : the mean softmax attention weight on designated patterns (\bar{a}_{des} , measured in continuous PCA space during sampling) and the fraction of decoded sequences with K/R at P1 (f_{obs} , measured after inverse PCA and argmax decoding). The attention weight tracked f_{eff} with $< 0.3\%$ deviation at all ρ values, consistent with Proposition 1: the energy-level conditioning worked as intended. However, the decoded phenotype fraction told a different story. P1 K/R fraction increased from 0.41 ($\rho = 1$) to only 0.63 ($\rho = 500$), far short of the $f_{\text{eff}} = 0.996$ that the attention weights achieved. This discrepancy between what the energy delivers in PCA space and what the decoder recovers in sequence space is the calibration gap. Sequence diversity decreased modestly from 0.56 to 0.51 over this range and KL divergence increased from 0.007 to 0.017. The phase transition β^* shifted from 4.4 at $\rho = 1$ ($K_{\text{eff}} = 99$) to 9.3 at $\rho = 1,000$ ($K_{\text{eff}} = 32.1$), and the entropy curves at different ρ values formed a family of sigmoidal profiles with systematically rightward-shifted inflection points, consistent with $\beta^*(\mathbf{r})$ depending on $K_{\text{eff}}(\mathbf{r})$ rather than the raw pattern count K (Fig. 2). To understand why f_{obs} lagged f_{eff} , we measured all three layers of the signal chain (Eq. 7) independently across a fine ρ sweep ($\rho \in [1, 1000]$, 17 values, 5 replicates each), recording at each step: (i) the total softmax attention weight on designated patterns (\bar{a}_{des}), (ii) the continuous K/R probability at P1 in the PCA-reconstructed one-hot vector (f_{soft}), and (iii) the hard-decoded residue identity (f_{obs}). We found that the attention gap was $\Delta_{\text{attn}} \approx 0$ across all ρ values ($< 0.3\%$), indicating that the energy-level conditioning was exact; the PCA gap was the dominant component, with f_{soft} effectively flat at ~ 0.27 regardless of ρ , varying by

less than 0.04 across a thousandfold range of multiplicity ratios; and the argmax gap was negative (≈ -0.25), indicating that discrete decoding partially recovered signal lost in the PCA reconstruction. These observations suggest that the PCA encoding mapped designated and background sequences to overlapping regions at the P1 position: even when 99.8% of attention weight was on the designated patterns, the continuous one-hot reconstruction could not resolve K vs. G at P1 because this variation was not well-captured by the top $d = 80$ principal components. The Fisher separation index for the Kunitz designated/background split was $S = 0.20$, consistent with moderate but incomplete geometric separation.

Cross-family validation and the separation index. We repeated the multiplicity analysis on four additional Pfam families (SH3 domains (PF00018; $K = 55$, split by conserved Trp at the binding groove), WW domains (PF00397; $K = 420$, split by specificity-loop residue), Homeobox domains (PF00046; $K = 136$, split by Gln at position 50 in the recognition helix), and Forkhead domains (PF00250; $K = 246$, split by His/Asn at the H3 recognition helix)), yielding five families with distinct PCA-space geometries (Table 1, Table 2). The calibration gap decreased monotonically with increasing separation index: WW domains ($S = 0.11$, functional subsets heavily interleaved in PCA space) exhibited the largest gap ($\Delta = 0.64$); Forkhead domains ($S = 0.17$) a moderate gap ($\Delta = 0.27$); Kunitz domains ($S = 0.20$) a similar gap ($\Delta = 0.39$); and both SH3 ($S = 0.34$, $\Delta = 0.01$) and Homeobox ($S = 0.42$, $\Delta = 0.04$) domains showed gaps near zero (Fig. 3). A linear fit across all five Pfam families yielded $\Delta \approx 0.72 - 1.8 S$ with $R^2 = 0.80$; the relationship is monotonic, with families above $S > 0.3$ achieving near-complete phenotype transfer via multiplicity weighting alone and families below $S < 0.2$ showing gaps of 0.27–0.64. Extending the multiplicity sweep to ω -conotoxin ($S = 0.78$, pharmacologically defined binder split) yielded $\Delta = 0.15$, consistent with the monotonic trend. The attention weights tracked f_{eff} closely in all six families, indicating that the multiplicity-weighted energy operates as expected regardless of the downstream calibration gap, while hard curation achieved 100% phenotype transfer in all families regardless of separation index, as expected since curated memory matrices are built from designated-subset-only PCA, which by construction captures subset-specific variation in its leading components. To test whether increasing β beyond β^* could push more phenotype signal through the PCA bottleneck, we swept β/β^* from 0.5 to 3.0 at three fixed ρ values ($\rho = 10, 50, 200$) on the Kunitz domain and observed a consistent tradeoff: higher β increased P1 K/R fraction at the cost of reduced diversity. At $\rho = 200$ and $\beta = 3\beta^*$, P1 K/R reached 0.71 (versus 0.61 at β^*) while diversity dropped from 0.53 to 0.46, suggesting that the practitioner can tune $(\rho, \beta/\beta^*)$ jointly to navigate the fidelity–diversity tradeoff.

Application to ω -conotoxin Cav2.2 binders. We applied SA to the ω -conotoxin O-superfamily (disulfide-rich peptides from predatory cone snails that block voltage-gated N-type calcium channels (Cav2.2) in sensory neurons [9]) to test whether curated memory conditioning generalizes beyond classical protein domains to therapeutically relevant peptide families (Table 5, Fig. 4). Cav2.2 mediates pain signaling in dorsal root ganglion (DRG) neurons, and channel block attenuates synaptic transmission between peripheral nociceptors and the spinal cord. This family has direct therapeutic relevance— ω -conotoxin MVIIA (ziconotide) is an FDA-approved non-opioid analgesic for intractable pain [10]—and is motivated by prior computational modeling of ATP-gated calcium dynamics in DRG neurons that identified Cav2.2 as a central node in the pain signaling network [11]. The primary Cav2.2 pharmacophore is Tyr13 (MVIIA numbering): the hydroxyl group contacts the channel pore directly and its substitution abolishes binding, while basic residues (Lys, Arg) distributed across the peptide contribute electrostatic complementarity with the negatively charged channel entrance. We compiled 74 SwissProt ω -conotoxin sequences, computed a multiple sequence alignment with MAFFT [12], retained 26 positions after gap filtering, designated 23 sequences as strong Cav2.2 binders (confirmed or predicted N-type channel blockers, including MVIIA, GVIA, CVID, CVIE, CVIF, and close homologs) and 2 sequences as weak or non-N-type-selective (MVIIC and MVIID, which preferentially block P/Q-type channels with $\text{IC}_{50} \geq 200$ nM against Cav2.2), and ran two independent SA experiments (50 chains \times 5000 steps, $\alpha = 0.01$), generating 1550 sequences per condition: one seeded from the full family ($K = 74$, $\beta^* = 3.23$) and one from the strong binders only ($K = 23$, $\beta^* = 2.72$). Pharmacophore inheritance was high under strong-binder seeding and attenuated under full-family seeding: in the full-family input only 33.8% of the 74 sequences carried Tyr at the pharmacophore position (col. 13), and full-family-seeded generation raised this modestly to 46.9%, whereas 82.6% of the 23 strong binders carried Tyr13 and strong-binder-seeded SA raised this to 98.3% (Table 5). The basic-residue (Lys + Arg) fraction was also preserved: strong-binder generation produced 20.1% basic residues versus 19.7% in the input, while

full-family generation produced only 12.0%, matching the lower K/R content of the diverse full-family input. Per-position amino acid frequency heatmaps showed the conditioning effect directly (Fig. 4): the strong-binder input and strong-binder-generated heatmaps were similar throughout, with Tyr at position 13, conserved Cys framework at positions 14–16, and variable-loop diversity at positions 9–12 all retained; the residual heatmaps (generated – input) showed small deviations across all positions, suggesting that SA reproduced the input frequency statistics rather than collapsing to a consensus sequence. Sequence-level inspection of the five highest-confidence strong-seeded sequences (ranked by ESMFold pLDDT) showed that all five preserved every highly conserved position (6/6), all six cysteines, and carried Tyr at the pharmacophore position, while introducing 5–11 substitutions at variable sites; the per-position entropy correlation between stored and strong-seeded sequences was $r = 0.745$, lower than the full-seeded correlation ($r = 0.997$), reflecting the reduced diversity at co-varying loop positions that contribute to Cav2.2 binding specificity (Fig. 6). We further validated the generated sequences against published structure–activity relationship (SAR) data by measuring agreement with experimentally identified binding determinants at 12 positions (Table 6): SA strong-seeded sequences preserved the primary pharmacophore (Tyr13: 98.3%), all six disulfide-forming cysteines ($\geq 97.4\%$), and enriched basic residues at loop 2 positions critical for channel interaction (Lys2: 97.5% K/R; Arg10: 82.3% K/R) relative to both the 23-sequence input and full-family generation, indicating that curated memory conditioning transferred both global pharmacophore statistics and the specific residue-level binding determinants identified by prior mutagenesis work [13–15]. Structural validation showed that the generated conotoxin sequences adopted the expected inhibitor cystine knot fold, with the disulfide-constrained loop architecture retained across all three top SA strong-seeded variants (Fig. 7). Together, these results indicate that curated memory conditioning transferred Cav2.2 pharmacophore statistics from a set of 23 characterized sequences to a library of 1 550 candidates, with no retraining and without requiring the Cav2.2 target structure for sequence generation.

AlphaFold2 multimer complex prediction. We tested whether SA-generated sequences produce complex-level predictions comparable to natural ω -conotoxins using ColabFold AlphaFold2-multimer with the Cav2.2 pore-domain target (Table 7). SA strong-conditioned ($n = 10$; pTM 0.221 ± 0.007 , iPTM 0.105 ± 0.008 , interface-pLDDT 37.2 ± 5.4) and SA full-conditioned ($n = 10$; pTM 0.219 ± 0.008 , iPTM 0.104 ± 0.007 , interface-pLDDT 38.2 ± 4.0) sequences were statistically indistinguishable from natural controls ($n = 5$; pTM 0.228 ± 0.004 , iPTM 0.108 ± 0.007 , interface-pLDDT 40.7 ± 3.5) on all four metrics (exact permutation tests; all $p > 0.05$). SA-generated sequences thus match natural ω -conotoxins under multimer prediction, indicating that the generation process does not degrade predicted binding geometry. The absolute scores are modest across all groups, reflecting the known difficulty of predicting small-peptide–channel complexes rather than a deficiency of the generated sequences; experimental binding assays remain necessary to assess functional activity.

Structural and linguistic validation. We predicted folds for 50 sequences from each source (stored, SA full-family, SA strong-conditioned, SA weak-conditioned, and HMM baseline) using ESMFold and computed TM-scores against the experimental Kunitz domain structure (1BPI, chain A) to verify that SA-generated sequences encode plausible three-dimensional structures (Table 3). We found that SA-generated sequences were structurally comparable to natural sequences: mean pLDDT was 90.4 ± 1.2 (SA full) and 90.7 ± 1.1 (SA strong) versus 89.3 ± 3.2 for stored sequences, with 100% of SA sequences exceeding the pLDDT > 70 confidence threshold; mean TM-scores were 0.84 ± 0.01 (SA full) and 0.83 ± 0.01 (SA strong) versus 0.83 ± 0.03 for stored sequences, all well above the TM > 0.5 same-fold threshold (Fig. 7); whereas HMM-emitted sequences achieved only 60.4 ± 13.1 mean pLDDT (20% above threshold) and 0.60 ± 0.10 mean TM-score, which suggests that profile HMM emission does not reliably produce foldable sequences (Table 3). AlphaFold2-ptm predictions via ColabFold [16, 17] were consistent with these results (Table 4): Kunitz TM-scores were 0.83–0.85 (pLDDT 93–95) and ω -conotoxin TM-scores were 0.35–0.47 (pLDDT 68–79) across stored and SA-generated sequences, consistent with the ESMFold values and the shorter peptide length of conotoxins. We further assessed sequence plausibility using ESM2-650M pseudo-perplexity computed via masked marginal scoring over all positions and found that SA-generated sequences achieved pseudo-perplexity comparable to natural sequences (SA full: 4.78 ± 0.64 ; SA strong: 4.72 ± 0.60 ; stored: 4.97 ± 0.98), while HMM-emitted sequences were approximately threefold worse (16.1 ± 4.2)—the slightly lower perplexity of conditioned SA sequences relative to stored sequences is consistent with SA’s tendency to generate near the center of the family distribution, away from outlier

sequences present in natural alignments (Table 3). We also compared SA against HMMER3 [6] profile HMM emission (150 sequences, `hmmemit -seed 42`) and bootstrap resampling from stored patterns and found that SA full-family generation preserved the natural P1 K/R proportion (0.41 ± 0.01) and achieved the lowest KL divergence (0.0069 ± 0.0001), while HMM emission produced sequences with lower P1 K/R fraction (0.15 ± 0.03) and higher compositional divergence (0.030 ± 0.011); bootstrap resampling preserved composition (KL ≈ 0.001) but produced no novel sequences; and SA strong-binder conditioning achieved complete P1 K/R fraction (1.0 ± 0.0)—a capability not available to unconditional baselines (Table 3). These results indicate that SA generated structurally valid, language-model-plausible sequences that exceeded classical baselines on both fidelity and functional conditioning.

3 Discussion

We have shown that pattern multiplicity in the modern Hopfield energy provides a principled, training-free mechanism for conditioning protein sequence generation on functional subsets. The theoretical framework is exact: multiplicity weights tilt the Boltzmann distribution through a simple logit bias, and the resulting Langevin dynamics sample from a known distribution with no approximation. A single scalar ρ continuously interpolates between unconditioned generation and hard subset curation, and the practitioner can compute the required ρ for any target effective designated fraction directly from the family composition (Eq. 4). On the Kunitz domain, curated memory achieved 100% phenotype transfer with as few as three designated input sequences; multiplicity-weighted generation on the full family increased phenotype fidelity from the natural proportion (32%) to 63% at $\rho = 500$; and the cross-family validation on five Pfam families showed a quantitative relationship between PCA-space geometry and conditioning effectiveness.

The central finding is the calibration gap and its decomposition. The gap is not a failure of the multiplicity-weighted energy (the attention weights track f_{eff} with $< 0.3\%$ deviation across all families and ρ values tested) but a well-characterized property of the PCA encoding that compresses $20L$ -dimensional sequence space into d principal components. When the designated and background subsets overlap in PCA space (low S), the energy-level tilt does not propagate to the decoded residue identity; when they separate (high S), it does. The cross-family validation across five Pfam families produced a monotonic negative relationship between S and Δ ($R^2 = 0.80$ for a linear fit), indicating that the separation index is a useful *a priori* predictor of conditioning effectiveness. This yields a practitioner’s decision rule: compute S (a cheap operation requiring only PCA and pairwise cosine similarities, no generation); if $S > 0.3$, multiplicity weighting preserves fold-level constraints from the full family while achieving high phenotype transfer (SH3 and Homeobox domains, $\Delta < 0.05$); if $S < 0.2$, hard curation is necessary because the PCA bottleneck attenuates the signal (WW and Forkhead domains, $\Delta = 0.27$ – 0.64); the intermediate regime ($0.2 < S < 0.3$, Kunitz domains) admits a tradeoff controlled by $(\rho, \beta/\beta^*)$.

Hard curation achieves complete phenotype transfer with as few as three designated input sequences. Many experimental campaigns (phage display, yeast surface display, functional selections, or even literature curation) produce exactly this kind of small, functionally characterized set. The practitioner brings external knowledge (“these sequences bind my target,” “these variants are thermostable,” “these hits came from my screen”) and SA converts this small set into a large, diverse candidate library while preserving the input phenotype. This “small-set amplifier” capability complements high-throughput screening: the screen identifies a few hits, SA expands them computationally, and the expanded library can be fed back into a second round of selection or directly into functional assays. The method itself is agnostic to the meaning of the designation; it biases the sampler toward the designated patterns regardless of whether the underlying phenotype is binding, stability, expression, or any other property. The scaling study shows that even $K_{\text{des}} = 3$ suffices for phenotype transfer; diversity improves with more input sequences but saturates near $K_{\text{des}} = 20$.

The ω -conotoxin experiment extends the small-set amplifier result to a therapeutically relevant peptide family and illustrates a practically important design choice: whether to seed SA from the full family or from a curated functional subset. Full-family seeding is appropriate when the goal is to generate novel family members with broad structural diversity; curated seeding is necessary when the goal is to preserve a specific pharmacophore. In the ω -conotoxin case, the O-superfamily is structurally coherent (all members share the C–C–CC–C–C disulfide framework) but functionally heterogeneous (members block N-type, P/Q-type, or sodium channels with varying selectivity).

Full-family seeding dilutes the Cav2.2-specific Tyr pharmacophore because the PCA encoding reflects the full structural diversity; curated seeding from the 23 N-type blockers concentrates the PCA subspace on Cav2.2-relevant variation, allowing SA to regenerate it with 98% fidelity. This generalizes the separation-index interpretation: even when S is moderate, hard curation can achieve high pharmacophore transfer by restricting the memory to the functional subset of interest. The cost (lower sequence diversity and reduced novelty, 0.46 vs. 0.60) reflects the narrower PCA basis, consistent with the Kunitz scaling study.

The AlphaFold2-multimer analysis shows that SA-generated ω -conotoxins are indistinguishable from natural sequences under complex prediction: all four metrics (pTM, iTM, confidence, interface pLDDT) overlap between generated and control groups with no significant differences. This is consistent with the structural and pharmacophore validation: generation preserves the properties that determine predicted binding geometry. The absolute scores are modest across all groups, a known limitation of multimer prediction for small-peptide-channel complexes; experimental binding assays are needed to determine whether the preserved pharmacophore translates to functional Cav2.2 block.

Several limitations should be acknowledged. The cross-family regression spans five Pfam families (plus ω -conotoxin) with $R^2 = 0.80$ for a linear fit; while the monotonic trend is clear, additional families would help characterize the functional form of the S - Δ relationship, which may be nonlinear (the gap appears to decay steeply below $S \approx 0.3$ and flatten near zero above it). Our functional splits are defined by single marker positions (P1 in Kunitz, Trp in SH3, specificity-loop residue in WW, Gln at position 50 in Homeobox, H/N at the recognition helix in Forkhead); multi-position phenotypes, where specificity depends on coordinated residue identities at several positions, may exhibit different calibration behavior. We have not experimentally validated the binding activity of generated sequences; the phenotype fidelity reported here is a necessary but not sufficient condition for functional binding. For the ω -conotoxin family, we validated SA-generated sequences against published SAR data from alanine-scanning and site-directed mutagenesis studies [13–15] and found that strong-seeded generation preserved all experimentally identified binding determinants (Table 6); for the Kunitz domain, deep mutational scanning data for the BPTI–trypsin interaction are now available [18] and could provide a quantitative binding-landscape comparison in future work. Computational binding affinity predictions (e.g., via AlphaFold-Multimer or FoldX) could provide an additional intermediate validation tier between sequence-level markers and experimental assays. Finally, we tested interface-weighted PCA encoding as a strategy to close the calibration gap, but found it neutral at low weights and destructive at high weights; the PCA bottleneck reflects the geometric entanglement of functional and structural variation in the family, not the absence of interface-position components.

Looking forward, the multiplicity framework opens several directions. The binary split (designated/background) generalizes naturally to multi-class conditioning by assigning different multiplicities to different functional categories. The PCA bottleneck that limits conditioning effectiveness might be reduced by alternative sequence encodings. Learned representations from protein language models, for instance, may better separate functional subsets than linear PCA. The β lever suggests that adaptive temperature schedules, increasing β during sampling to sharpen the multiplicity bias, could improve phenotype transfer without permanently sacrificing diversity. These extensions remain within the analytic, training-free framework that makes stochastic attention practical for the scarce-data regime.

4 Materials and Methods

4.1 From Hopfield Energy to Multiplicity-Weighted Score Function

Let $\mathbf{X} = [\mathbf{m}_1, \dots, \mathbf{m}_K] \in \mathbb{R}^{d \times K}$ be a memory matrix whose columns are unit-norm, PCA-encoded protein sequences from a family alignment of K members, each represented in d dimensions. The modern Hopfield energy [19] at state $\boldsymbol{\xi} \in \mathbb{R}^d$ is $E(\boldsymbol{\xi}) = \frac{1}{2} \|\boldsymbol{\xi}\|^2 - \frac{1}{\beta} \log \sum_k \exp(\beta \mathbf{m}_k^\top \boldsymbol{\xi})$, where $\beta > 0$ is an inverse temperature. The score function $\nabla_{\boldsymbol{\xi}} \log p_{\beta}(\boldsymbol{\xi}) = \mathbf{X} \text{softmax}(\beta \mathbf{X}^\top \boldsymbol{\xi}) - \boldsymbol{\xi}$ is *exact* and computed by a single attention operation; applying the unadjusted Langevin algorithm (ULA) with step size $\alpha \in (0, 1)$ yields the stochastic attention update [7]:

$$\boldsymbol{\xi}_{t+1} = (1 - \alpha) \boldsymbol{\xi}_t + \alpha \mathbf{X} \text{softmax}(\beta \mathbf{X}^\top \boldsymbol{\xi}_t) + \sqrt{2\alpha/\beta} \boldsymbol{\epsilon}_t, \quad \boldsymbol{\epsilon}_t \sim \mathcal{N}(\mathbf{0}, \mathbf{I}_d). \quad (1)$$

We extend this framework to condition generation on a functional subset by assigning a multiplicity weight $r_k > 0$ to each stored pattern. The *multiplicity-weighted* Hopfield energy is

$$E_{\mathbf{r}}(\boldsymbol{\xi}) = \frac{1}{2} \|\boldsymbol{\xi}\|^2 - \frac{1}{\beta} \log \sum_{k=1}^K r_k \exp(\beta \mathbf{m}_k^\top \boldsymbol{\xi}), \quad (2)$$

where $\mathbf{r} = (r_1, \dots, r_K)^\top$. When $r_k = 1$ for all k , Eq. (2) reduces to the standard energy. Patterns with higher multiplicity deepen the energy wells in their vicinity; this is equivalent to storing r_k copies of pattern \mathbf{m}_k without the $\mathcal{O}(d \cdot \sum_k r_k)$ memory cost.

Proposition 1 (Score function). *The score function of $p_{\mathbf{r}}(\boldsymbol{\xi}) \propto \exp(-\beta E_{\mathbf{r}}(\boldsymbol{\xi}))$ is $\nabla_{\boldsymbol{\xi}} \log p_{\mathbf{r}}(\boldsymbol{\xi}) = \mathbf{X} \text{softmax}(\beta \mathbf{X}^\top \boldsymbol{\xi} + \log \mathbf{r}) - \boldsymbol{\xi}$, where $\log \mathbf{r} = (\log r_1, \dots, \log r_K)^\top$ is the elementwise log-multiplicity.*

The proof follows from the identity $r_k \exp(a_k) = \exp(a_k + \log r_k)$: the weights are absorbed into the softmax logits. The resulting Langevin update is

$$\boldsymbol{\xi}_{t+1} = (1 - \alpha) \boldsymbol{\xi}_t + \alpha \mathbf{X} \text{softmax}(\beta \mathbf{X}^\top \boldsymbol{\xi}_t + \log \mathbf{r}) + \sqrt{2\alpha/\beta} \boldsymbol{\epsilon}_t. \quad (3)$$

The *only* change from Eq. (1) is the addition of $\log r_k$ to each logit before the softmax. The memory matrix \mathbf{X} is unchanged, the noise schedule is unchanged, and the sampler retains its $\mathcal{O}(dK)$ per-step cost.

4.2 Multiplicity Ratio and Phase Transition

For a binary functional split (designated subset vs. background), we parameterize the multiplicity vector by a single scalar $\rho = r_{\text{designated}}/r_{\text{background}}$, setting $r_k = \rho$ for patterns in the user-designated subset and $r_k = 1$ otherwise. The effective designated fraction (the share of the softmax probability mass attributable to designated patterns when all patterns have equal similarity to $\boldsymbol{\xi}$) is $f_{\text{eff}}(\rho) = K_{\text{des}}\rho/(K_{\text{des}}\rho + K_{\text{bg}})$, where K_{des} and $K_{\text{bg}} = K - K_{\text{des}}$ are the number of designated and background patterns. At $\rho = 1$, $f_{\text{eff}} = K_{\text{des}}/K$; as $\rho \rightarrow \infty$, $f_{\text{eff}} \rightarrow 1$. Inverting gives the multiplicity ratio needed for a target fraction f :

$$\rho(f) = \frac{f \cdot K_{\text{bg}}}{K_{\text{des}}(1 - f)}. \quad (4)$$

The standard SA framework exhibits a phase transition at critical inverse temperature β^* that depends on the PCA dimension d and the number of stored patterns. Under multiplicity weighting, the relevant quantity is the effective number of patterns $K_{\text{eff}}(\mathbf{r}) = (\sum_k r_k)^2 / \sum_k r_k^2$, which equals K when all r_k are equal and converges to K_{des} as $\rho \rightarrow \infty$.

Remark 2 (Phase transition: analytic baseline and multiplicity shift). The companion paper [7] establishes, via a concentration-of-measure argument on the softmax attention entropy, that for the *unweighted* SA sampler ($\rho = 1$) the phase transition satisfies

$$\beta^* \approx 1.57 + 0.28\sqrt{d}, \quad (5)$$

with $R^2 = 0.97$ across eight Pfam families spanning $d \in [18, 186]$, and is nearly independent of K for $K \geq 30$. At $\rho = 1$, Eq. (5) therefore gives the analytic value directly from the alignment. For $\rho > 1$, the logit biases $\log r_k$ pre-concentrate the attention distribution at $\beta = 0$: the weighted entropy at zero temperature is $H_{\mathbf{r}}(0) = \log K_{\text{eff}}(\mathbf{r}) < \log K$, a lower starting entropy than the unweighted case. Reaching the retrieval-phase inflection from this pre-concentrated starting point requires a higher inverse temperature, so $\beta^*(\rho) \geq \beta^*(1)$. For intermediate ρ , $\beta^*(\rho)$ is located as the inflection of the weighted attention entropy $H_{\mathbf{r}}(\beta)$ via a one-dimensional sweep, a negligible computation relative to sequence generation.

Empirically, β^* increases monotonically from 4.4 ($\rho = 1$, $K_{\text{eff}} = 99$) to 9.3 ($\rho = 1000$, $K_{\text{eff}} = 32.1$) in the Kunitz domain, consistent with Remark 2: more inverse temperature is required as the logit biases concentrate probability mass on fewer effective patterns.

4.3 The Calibration Gap

The signal chain from multiplicity weights to decoded sequence phenotype passes through several transformations:

$$\rho \xrightarrow{\text{exact}} f_{\text{eff}} \xrightarrow{\text{exact}} \bar{a}_{\text{des}} \xrightarrow{\text{lossy}} f_{\text{soft}} \xrightarrow{\text{nonlinear}} f_{\text{obs}}, \quad (6)$$

where \bar{a}_{des} is the mean attention weight on designated patterns during sampling, f_{soft} is the continuous-valued residue probability at the marker position, and f_{obs} is the fraction of generated sequences displaying the designated phenotype after argmax decoding. We define the calibration gap $\Delta = f_{\text{eff}} - f_{\text{obs}}$ and decompose it into three independently measurable components:

$$\Delta = \underbrace{(f_{\text{eff}} - \bar{a}_{\text{des}})}_{\Delta_{\text{attn}} \approx 0} + \underbrace{(\bar{a}_{\text{des}} - f_{\text{soft}})}_{\Delta_{\text{PCA}}} + \underbrace{(f_{\text{soft}} - f_{\text{obs}})}_{\Delta_{\text{argmax}}}. \quad (7)$$

To predict the PCA gap across families, we define the Fisher separation index $S = (\bar{c}_{\text{within}} - \bar{c}_{\text{between}}) / [\frac{1}{2}(\sigma_{\text{within}} + \sigma_{\text{between}})]$, where \bar{c} and σ denote the mean and standard deviation of pairwise cosine similarities within and between functional groups in PCA space. For each experiment, we followed the stochastic attention pipeline of [7] without modification to the core sampler. Seed alignments were downloaded from InterPro/Pfam in Stockholm format (or, for the ω -conotoxin O-superfamily, compiled from SwissProt and aligned with MAFFT [12]). Alignments were cleaned by removing columns with > 50% gaps and sequences with > 30% gaps in the remaining columns. The cleaned alignment was one-hot encoded (20 amino acid channels per position, gaps mapped to zero vectors) yielding a $20L \times K$ matrix, reduced by PCA (retaining 95% of variance) to a $d \times K$ matrix, and column-normalized to unit norm. ULA chains were run with step size $\alpha = 0.01$ for $T = 5,000$ steps, initialized near random stored patterns with small Gaussian perturbation; samples were collected after a burn-in of 2,000 steps with thinning every 100 steps. We tested five Pfam families (Kunitz domains (PF00014, $K = 99$, $L = 53$), SH3 domains (PF00018, $K = 55$, $L = 48$), WW domains (PF00397, $K = 420$, $L = 31$), Homeobox domains (PF00046, $K = 136$, $L = 57$), and Forkhead domains (PF00250, $K = 246$, $L = 87$)) and the ω -conotoxin O-superfamily ($K = 74$, $L = 26$, curated from SwissProt). For each family, we defined a binary functional split based on a single marker position reflecting external biological knowledge, not a property discovered by the method: for Kunitz, the P1 position (primary contact residue with serine proteases) was identified as the column with the highest Lys frequency and sequences with K or R at P1 were designated as the functional subset ($K_{\text{des}} = 32$); for SH3, the conserved Trp in the hydrophobic binding groove was the marker ($K_{\text{des}} = 33$); for WW, the specificity-determining position was the highest-entropy column in the middle third of the alignment ($K_{\text{des}} = 69$); for Homeobox, Gln at position 50 in the recognition helix (the primary determinant of TAAT-core DNA-binding specificity) was the marker ($K_{\text{des}} = 102$); for Forkhead, His or Asn at the H3 recognition helix position (residues that make base-specific contacts in the major groove) was the marker ($K_{\text{des}} = 122$); and for ω -conotoxin, 23 confirmed or predicted N-type Cav2.2 blockers were designated as strong binders based on pharmacological characterization [9].

For multiplicity-weighted runs, the multiplicity vector was set to $r_k = \rho$ for designated patterns and $r_k = 1$ for background patterns, and $\beta^*(\mathbf{r})$ was found by sweeping 50–60 logarithmically spaced β values in $[0.1, 500]$ and locating the inflection point of the weighted attention entropy. Twenty to fifty independent chains were run per condition, yielding 620–1,550 sequences after burn-in and thinning. Phenotype fidelity was measured as the fraction of generated sequences displaying the designated marker residue at the marker position; attention diagnostics recorded the mean softmax weight on designated patterns during sampling; sequence diversity was computed as one minus the mean pairwise sequence identity (estimated from 300–500 random pairs); and amino acid composition fidelity was measured by KL divergence between generated and reference amino acid frequencies. The Fisher separation index S was computed from pairwise cosine similarities between unit-norm PCA vectors within and between functional groups as defined in Section 4.3. Structural validation used ESMFold [5] to predict structures for 50 sequences per source, with pLDDT extracted from the B-factor column and TM-scores computed against experimental reference structures (1BPI chain A for Kunitz, 1OMG chain A for ω -conotoxin) using TM-align [20]; these results were independently cross-validated with AlphaFold2-ptm via ColabFold [16, 17] (1 model, 3 recycles, MMseqs2 MSA, no relaxation) run on Google Colab with a T4 GPU. Sequence plausibility was assessed using ESM2-650M pseudo-perplexity computed via masked marginal scoring over all positions [5]. All experiments were implemented in Julia 1.12 using NNlib.jl (softmax), MultivariateStats.jl (PCA),

and Distributions.jl; source code and experiment scripts are available at <https://github.com/varnerlab/SA-Binding-Generation-Study>.

Acknowledgments

The author thanks the Cornell Center for Advanced Computing for computational resources.

Author contributions. J.D.V. conceived the study, developed the theory, wrote the code, performed the experiments, and wrote the paper.

Competing interests. The author declares no competing interests.

Data availability. All Pfam seed alignments are publicly available from InterPro. Source code and experiment scripts are available at <https://github.com/varnerlab/SA-Binding-Generation-Study>.

References

- [1] Kevin K. Yang, Zachary Wu, and Frances H. Arnold. Machine-learning-guided directed evolution for protein engineering. *Nature Methods*, 16:687–694, 2019.
- [2] Ali Madani, Ben Krause, Eric R. Greene, Subu Subramanian, Benjamin P. Mohr, James M. Holton, Jose Luis Olmos, Caiming Xiong, Zhi Zhong Sun, Richard Socher, James S. Fraser, and Nikhil Naik. Large language models generate functional protein sequences across diverse families. *Nature Biotechnology*, 41:1099–1106, 2023.
- [3] Sarah Alamdari, Nitya Thakkar, Rianne van den Berg, Alex X. Lu, Nicolo Fusi, Ava P. Amini, and Kevin K. Yang. Protein generation with evolutionary diffusion: sequence is all you need. *bioRxiv*, 2023. doi: 10.1101/2023.09.11.556673.
- [4] Justas Dauparas, Ivan Anishchenko, Nathaniel Bennett, Hua Bai, Robert J. Ragotte, Lukas F. Milles, Basile I. M. Wicky, Alexis Courbet, Rob J. de Haas, Neville Bethel, Philip J. L. Leung, Timothy F. Huddy, Sam Pellock, Doug Tischer, Frederick Chan, Brian Koepnick, Hannah Nguyen, Alex Kang, Banumathi Sankaran, Asim K. Bera, Neil P. King, and David Baker. Robust deep learning-based protein sequence design using ProteinMPNN. *Science*, 378:49–56, 2022.
- [5] Zeming Lin, Halil Akin, Roshan Rao, Brian Hie, Zhongkai Zhu, Wenting Lu, Nikita Smetanin, Robert Verkuil, Ori Kabeli, Yaniv Shmueli, Allan dos Santos Costa, Maryam Fazel-Zarandi, Tom Sercu, Sal Candido, and Alexander Rives. Evolutionary-scale prediction of atomic-level protein structure with a language model. *Science*, 379(6637):1123–1130, 2023.
- [6] Simon C Potter, Aurélien Luciani, Sean R Eddy, Youngmi Park, Rodrigo Lopez, and Robert D Finn. HMMER web server: 2018 update. *Nucleic acids research*, 46:W200–W204, 2018.
- [7] Jeffrey D. Varner. Training-free generation of protein sequences from small family alignments via stochastic attention. *arXiv preprint arXiv:2603.14717*, 2026. doi: 10.48550/arXiv.2603.14717.
- [8] Michael Laskowski and Izydor Kato. Protein inhibitors of proteinases. *Annual Review of Biochemistry*, 49:593–626, 1980.
- [9] Christina I. Schroeder and Richard J. Lewis. ω -conotoxins GVIA, MVIIA and CVID: SAR and clinical potential. *Marine Drugs*, 4(3):193–214, 2006.
- [10] George P. Miljanich. Ziconotide: neuronal calcium channel blocker for treating severe chronic pain. *Current Medicinal Chemistry*, 11(23):3029–3040, 2004.
- [11] Sang Ok Song and Jeffrey Varner. Modeling and analysis of the molecular basis of pain in sensory neurons. *PLOS ONE*, 4(9):e6758, 2009.

- [12] Kazutaka Katoh and Daron M. Standley. MAFFT multiple sequence alignment software version 7: improvements in performance and usability. *Molecular Biology and Evolution*, 30(4): 772–780, 2013.
- [13] J. I. Kim, M. Takahashi, A. Ohtake, A. Wakamiya, and K. Sato. Tyr13 is essential for the activity of omega-conotoxin MVIIA and GVIA, specific N-type calcium channel blockers. *Biochemical and Biophysical Research Communications*, 206(2):449–454, 1995.
- [14] K. Sato, N. G. Park, T. Kohno, T. Maeda, J. I. Kim, R. Kato, and M. Takahashi. Role of basic residues for the binding of omega-conotoxin GVIA to N-type calcium channels. *Biochemical and Biophysical Research Communications*, 194(3):1292–1296, 1993.
- [15] R. J. Lewis, S. Dutertre, I. Vetter, and M. J. Christie. Conus venom peptide pharmacology. *Pharmacological Reviews*, 64(2):259–298, 2012.
- [16] John Jumper et al. Highly accurate protein structure prediction with AlphaFold. *Nature*, 596: 583–589, 2021.
- [17] Milot Mirdita, Konstantin Schütze, Yoshitaka Moriwaki, Lim Heo, Sergey Ovchinnikov, and Martin Steinegger. ColabFold: making protein folding accessible to all. *Nature Methods*, 19: 679–682, 2022.
- [18] M. Heyne, J. Shirian, I. Cohen, Y. Peleg, E. S. Radisky, N. Papo, and J. M. Shifman. Climbing up and down binding landscapes through deep mutational scanning of three homologous protein–protein complexes. *Journal of the American Chemical Society*, 143(41):17261–17275, 2021.
- [19] Hubert Ramsauer, Bernhard Schöfl, Johannes Lehner, Philipp Seidl, Michael Widrich, Thomas Adler, Lukas Gruber, Markus Holzleitner, Milena Pavlović, Geir Kjetil Sandve, et al. Hopfield networks is all you need. *International Conference on Learning Representations*, 2021.
- [20] Yang Zhang and Jeffrey Skolnick. TM-align: a protein structure alignment algorithm based on the TM-score. *Nucleic Acids Research*, 33(7):2302–2309, 2005.
- [21] K. Sato, C. Raymond, N. Martin-Moutot, T. Sasaki, A. Ohtake, K. Minami, C. Van Renterghem, J. I. Kim, M. Takahashi, and M. J. Seagar. Binding of Ala-scanning analogs of omega-conotoxin MVIIIC to N- and P/Q-type calcium channels. *FEBS Letters*, 469(2–3):147–150, 2000.
- [22] C. I. Schroeder, K. J. Nielsen, D. A. Adams, M. Loughnan, L. Thomas, P. F. Alewood, R. J. Lewis, and D. J. Craik. Effects of Lys2 to Ala2 substitutions on the structure and potency of omega-conotoxins MVIIA and CVID. *Biopolymers*, 98(4):345–356, 2012.
- [23] C. I. Schroeder, M. L. Smythe, R. J. Lewis, and D. J. Craik. Effects of chirality at Tyr13 on the structure–activity relationships of omega-conotoxins from *Conus magus*. *Biochemistry*, 38(5): 1440–1446, 1999.

Table 1: **Cross-family summary of all protein families tested.** For each family: source database, number of sequences (K), aligned length (L), PCA dimensionality (d , capturing 95% variance), designated subset size (K_{des}), phenotype marker, natural designated fraction (f_{nat}), Fisher separation index (S), observed phenotype fraction under hard curation ($f_{\text{obs}}^{\text{hard}}$), and calibration gap (Δ at $\rho = 500$). All six families were tested with both multiplicity weighting and hard curation.

Family	Source	K	L	d	K_{des}	Marker	f_{nat}	S	$f_{\text{obs}}^{\text{hard}}$	Δ
WW	PF00397	420	31	186	69	Spec. loop	0.16	0.11	1.00	0.64
Forkhead	PF00250	246	87	172	122	H/N at H3	0.50	0.17	1.00	0.27
Kunitz	PF00014	99	53	80	32	P1 K/R	0.32	0.20	1.00	0.39
SH3	PF00018	55	48	46	33	Trp	0.60	0.34	1.00	0.01
Homeobox	PF00046	136	57	101	102	Gln at pos. 50	0.75	0.42	1.00	0.04
ω -Conotoxin	SwissProt	74	26	34	23	Tyr13	0.31	0.78	0.98	0.15

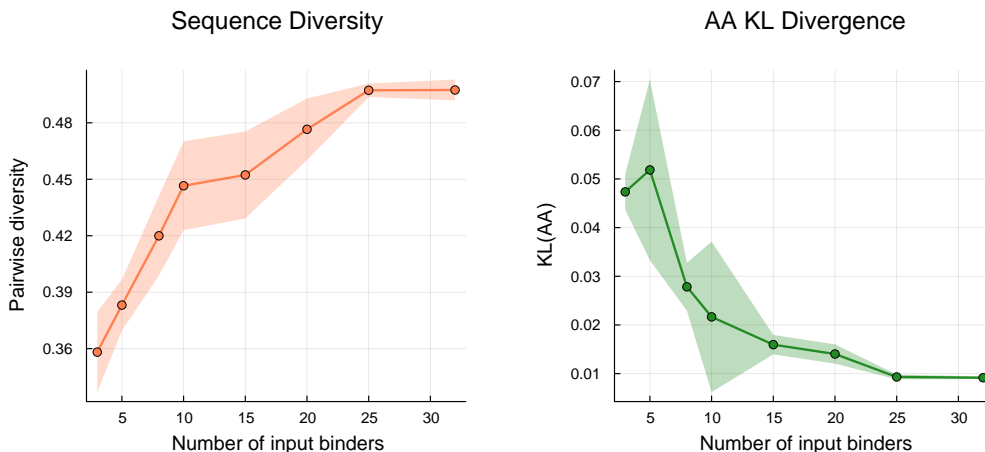


Figure 1: **Diversity and composition fidelity improve with more input binders; phenotype fidelity is perfect at every sample size.** Subsampling $K_{\text{des}} \in \{3, 5, 8, 10, 15, 20, 25, 32\}$ sequences from the Kunitz strong-binder set (3 replicates each; shaded bands show ± 1 s.d.). P1 K/R fraction was 1.0 at every sample size (not shown). *Left:* Pairwise sequence diversity increases from 0.36 ($K_{\text{des}} = 3$) to 0.50 ($K_{\text{des}} = 32$). *Right:* KL divergence of amino acid composition decreases from 0.047 to 0.009 over the same range. Three input binders suffice for perfect phenotype transfer; more binders improve the compositional and diversity quality of the generated library.

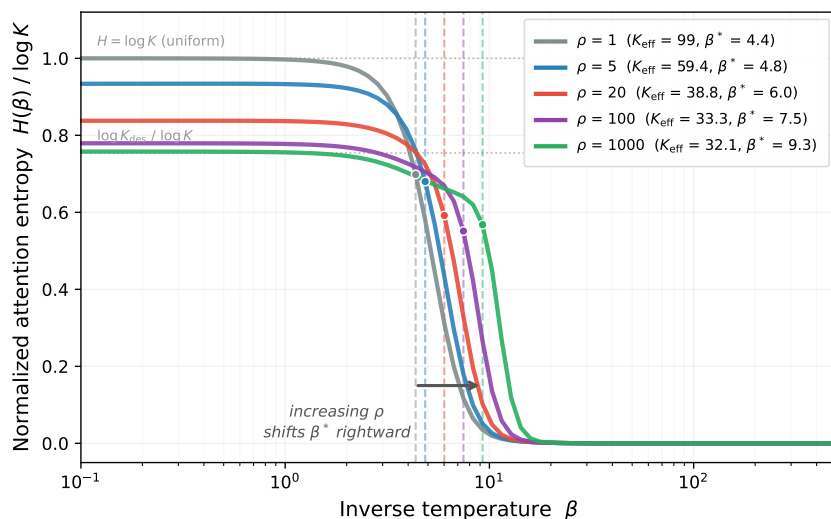


Figure 2: **Phase transition shifts rightward with increasing multiplicity ratio ρ .** Attention entropy $H(\beta)$ normalized by $\log K$ (the uniform limit) as a function of inverse temperature β (log scale) for $\rho \in \{1, 5, 20, 100, 1000\}$ on the Kunitz family ($K = 99$, $K_{\text{des}} = 32$). At $\rho = 1$ (standard SA), the entropy starts at $H/\log K = 1$ (uniform attention over all patterns); as ρ increases, the multiplicity bias pre-concentrates the attention distribution, lowering the starting entropy toward $\log K_{\text{des}}/\log K \approx 0.75$ (dotted line). Each curve shows a sigmoidal drop to near-zero entropy (retrieval phase); dots and dashed vertical lines mark the inflection point $\beta^*(\rho)$. As ρ increases from 1 to 1000, K_{eff} decreases from 99 to 32.1 and β^* shifts rightward from 4.4 to 9.3, consistent with fewer effective attractors requiring higher inverse temperature to produce an ordered phase.

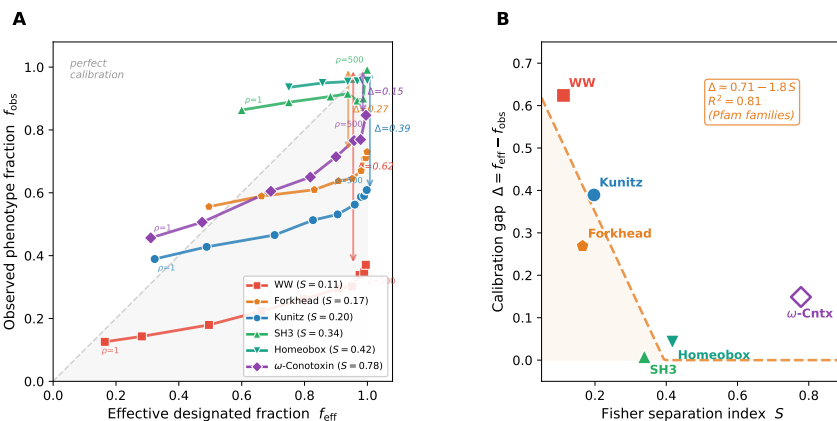


Figure 3: **Calibration trajectories reveal family-dependent gaps predicted by PCA-space separation.** (A) Observed phenotype fraction f_{obs} versus effective designated fraction f_{eff} as the multiplicity ratio ρ increases from 1 to 500 for six protein families. The dashed diagonal marks perfect calibration ($f_{\text{obs}} = f_{\text{eff}}$). Homeobox ($S = 0.42$) and SH3 ($S = 0.34$) domains track the diagonal closely; Kunitz ($S = 0.20$) and Forkhead ($S = 0.17$) curve below; WW domains ($S = 0.11$) show the largest departure; ω -conotoxin ($S = 0.78$) shows a moderate gap despite high PCA separation. Double-headed arrows indicate the calibration gap at $\rho = 500$. (B) Fisher separation index S versus calibration gap Δ at $\rho = 500$. A linear fit to the five Pfam families (filled markers; $\Delta \approx 0.72 - 1.8 S$, $R^2 = 0.80$) shows that the gap is predicted by the geometric separation of functional subsets in PCA space: families with $S > 0.3$ have gaps near zero, while families with $S < 0.2$ have gaps of 0.27–0.64. The ω -conotoxin point (open diamond) follows the monotonic trend.

Table 2: **Per-family ρ sweep: attention weights track f_{eff} exactly; decoded phenotype fidelity depends on PCA separation.** Selected ρ values for each family. f_{eff} : effective designated fraction from multiplicity weights; \bar{a}_{des} : mean softmax attention on designated patterns; f_{obs} : hard-decoded phenotype fraction (930 sequences); D : mean pairwise diversity. In all families $\bar{a}_{\text{des}} \approx f_{\text{eff}}$ (energy conditioning is exact), but f_{obs} converges fastest for Homeobox ($S = 0.42$) and slowest for WW ($S = 0.11$), reflecting the PCA-space calibration gap.

Family	(K, K_{des}, S)	ρ	f_{eff}	\bar{a}_{des}	f_{obs}	Δ	D
WW (PF00397)	(420, 69, 0.11)	1	0.164	0.156	0.126	0.04	0.682
		10	0.663	0.653	0.224	0.44	0.667
		100	0.952	0.951	0.302	0.65	0.653
		1000	0.995	0.996	0.371	0.62	0.618
Forkhead (PF00250)	(246, 122, 0.17)	1	0.496	0.490	0.556	-0.06	0.480
		10	0.908	0.904	0.638	0.27	0.447
		100	0.990	0.988	0.710	0.28	0.417
		1000	0.999	0.999	0.730	0.27	0.398
Kunitz (PF00014)	(99, 32, 0.20)	1	0.323	0.319	0.389	-0.07	0.563
		10	0.827	0.827	0.513	0.31	0.543
		100	0.979	0.981	0.587	0.39	0.523
		1000	0.998	0.998	0.609	0.39	0.512
SH3 (PF00018)	(55, 33, 0.34)	1	0.600	0.621	0.863	-0.26	0.587
		10	0.938	0.944	0.915	0.02	0.583
		100	0.993	0.994	0.980	0.01	0.532
		1000	0.999	0.999	0.991	0.01	0.519
Homeobox (PF00046)	(136, 102, 0.42)	1	0.750	0.758	0.935	-0.19	0.525
		10	0.968	0.969	0.955	0.01	0.522
		100	0.997	0.997	0.957	0.04	0.521
		1000	1.000	1.000	0.957	0.04	0.521
ω -Cntx (SwissProt)	(74, 23, 0.78)	1	0.311	0.299	0.456	-0.15	0.557
		10	0.819	0.809	0.650	0.17	0.516
		100	0.978	0.972	0.769	0.21	0.470
		500	0.996	0.994	0.847	0.15	0.435

Table 3: **Structural, linguistic, and functional validation on the Kunitz domain.** pLDDT: ESM-Fold predicted confidence (0–100; > 70 = confident). TM: TM-score against 1BPI chain A (> 0.5 = same fold). PPL: ESM2-650M masked-marginal pseudo-perplexity (lower = more plausible). P1 K/R: fraction with Lys/Arg at the primary trypsin contact. KL: amino acid composition divergence ($\times 10^3$). D : mean pairwise diversity. Structural and LM values are mean \pm s.d. across 50 sequences; sequence-level metrics are mean \pm s.d. across 5 replicates. SA-generated sequences are indistinguishable from natural sequences on all structural and linguistic metrics; SA strong-conditioning achieves perfect phenotype transfer, a capability unavailable to unconditional baselines.

Source	pLDDT	TM	PPL	P1 K/R	KL ($\times 10^3$)	D
Stored (natural)	89.3 \pm 3.2	0.83 \pm 0.03	4.97 \pm 0.98	0.32	0	0.63
SA (full family)	90.4 \pm 1.2	0.84 \pm 0.01	4.78 \pm 0.64	0.41 \pm 0.01	6.9 \pm 0.1	0.56
SA (strong binders)	90.7 \pm 1.1	0.83 \pm 0.01	4.72 \pm 0.60	1.00 \pm 0.00	19.5 \pm 0.4	0.50
SA (weak binders)	91.0 \pm 1.2	0.85 \pm 0.01	4.73 \pm 0.72	0.00 \pm 0.00	12.4 \pm 0.3	0.53
HMM emit (HMMER3)	60.4 \pm 13.1	0.60 \pm 0.10	16.1 \pm 4.2	0.15 \pm 0.03	29.7 \pm 11.3	0.56
Bootstrap (resample)	—	—	—	0.30 \pm 0.04	1.0 \pm 0.3	0.56

Table 4: **AlphaFold2-ptm cross-validation of structural quality.** Independent structure predictions via ColabFold (AlphaFold2-ptm, 1 model, 3 recycles, MMseqs2 MSA) for 50 sequences per source. pLDDT: mean predicted confidence (0–100). TM: TM-score against experimental reference (1BPI chain A for Kunitz, 1OMG chain A for ω -conotoxin). AF2 confirms the ESMFold results: SA-generated Kunitz sequences match or exceed stored sequences on both metrics; conotoxin TM-scores are lower overall, consistent with the 26-residue peptide length, but SA strong-seeded sequences achieve the highest pLDDT and TM-scores in both families.

Family	Source	n	pLDDT	TM-score
Kunitz	Stored (natural)	50	93.5 ± 4.0	0.83 ± 0.03
	SA (strong binders)	50	94.6 ± 1.4	0.84 ± 0.01
	SA (full family)	50	95.0 ± 1.3	0.85 ± 0.01
ω -Conotoxin	Stored (natural)	50	67.9 ± 9.8	0.35 ± 0.11
	SA (strong binders)	50	78.5 ± 4.1	0.47 ± 0.02
	SA (full family)	50	73.9 ± 10.4	0.39 ± 0.12

Table 5: **ω -Conotoxin Cav2.2 pharmacophore inheritance under curated vs. full-family seeding.** Tyr13%: fraction with tyrosine at the primary pharmacophore position (col. 13). K+R%: basic residue fraction (electrostatic complementarity). KL: amino acid composition divergence. Novelty: mean cosine distance to nearest stored pattern. Strong-binder seeding amplifies Tyr13 from 82.6% to 98.3% and preserves the basic-residue signature exactly, while full-family seeding dilutes both signals.

Condition	N	Tyr13 (%)	K+R (%)	KL	Novelty
Input: full family	74	33.8	9.9	0	0
Input: strong binders	23	82.6	19.7	0	0
Generated: full-seeded	1550	46.9	12.0	0.0075	0.60
Generated: strong-seeded	1550	98.3	20.1	0.0083	0.46

Table 6: **SA-generated ω -conotoxin sequences preserve experimentally validated binding determinants.** Published structure–activity relationship (SAR) data for ω -conotoxin binding to Cav2.2 identify critical residues whose mutation abolishes or substantially reduces channel block [13, 14, 21, 22, 15, 23]. For each SAR-critical position, the table reports the fraction of sequences that retain the wild-type residue (or a conservative K/R substitution for basic positions). SA strong-seeded generation preserves the primary pharmacophore (Tyr13: 98.3%) and all six cysteines ($\geq 97.4\%$), while enriching basic residues at functionally important loop 2 positions relative to the input.

Pos.	WT	Role	Mutation effect	Input	SA strong	SA full
13	Tyr	Primary pharmacophore	Ala: abolishes activity	0.83	0.98	0.47
2	Lys	Loop 2 stabilization	Ala: 40 \times loss (GVIA)	0.96	0.98	0.46
10	Arg	Loop 2 binding	Critical for interaction	0.70	0.82	0.35
11	Leu	Loop 2 binding	Critical for interaction	0.17	0.24	0.11
1	Cys	Disulfide framework	Required for fold	1.00	1.00	1.00
8	Cys	Disulfide framework	Required for fold	1.00	1.00	1.00
15	Cys	Disulfide framework	Required for fold	1.00	0.97	1.00
16	Cys	Disulfide framework	Required for fold	0.87	1.00	1.00
20	Cys	Disulfide framework	Required for fold	0.70	1.00	1.00
25	Cys	Disulfide framework	Required for fold	0.52	1.00	1.00
21	Arg	Electrostatic	Ala: reduced potency	0.44	0.66	0.14
4	Lys	P/Q selectivity	Ala: important for P/Q	0.52	0.61	0.28

Table 7: **AlphaFold2 multimer complex prediction validation for SA-generated ω -conotoxins.** Complex-level scores for sequences docked with Cav2.2 pore domain via ColabFold in multimer mode. For each group we report mean values and standard deviation of pTM, iPTM, and interface pLDDT.

Group	n	Mean pTM	Mean iPTM	Mean Interface pLDDT
SA strong-conditioned	10	0.221 \pm 0.007	0.105 \pm 0.008	37.2 \pm 5.4
SA full-conditioned	10	0.219 \pm 0.008	0.104 \pm 0.007	38.2 \pm 4.0
Natural controls	5	0.228 \pm 0.004	0.108 \pm 0.007	40.7 \pm 3.5

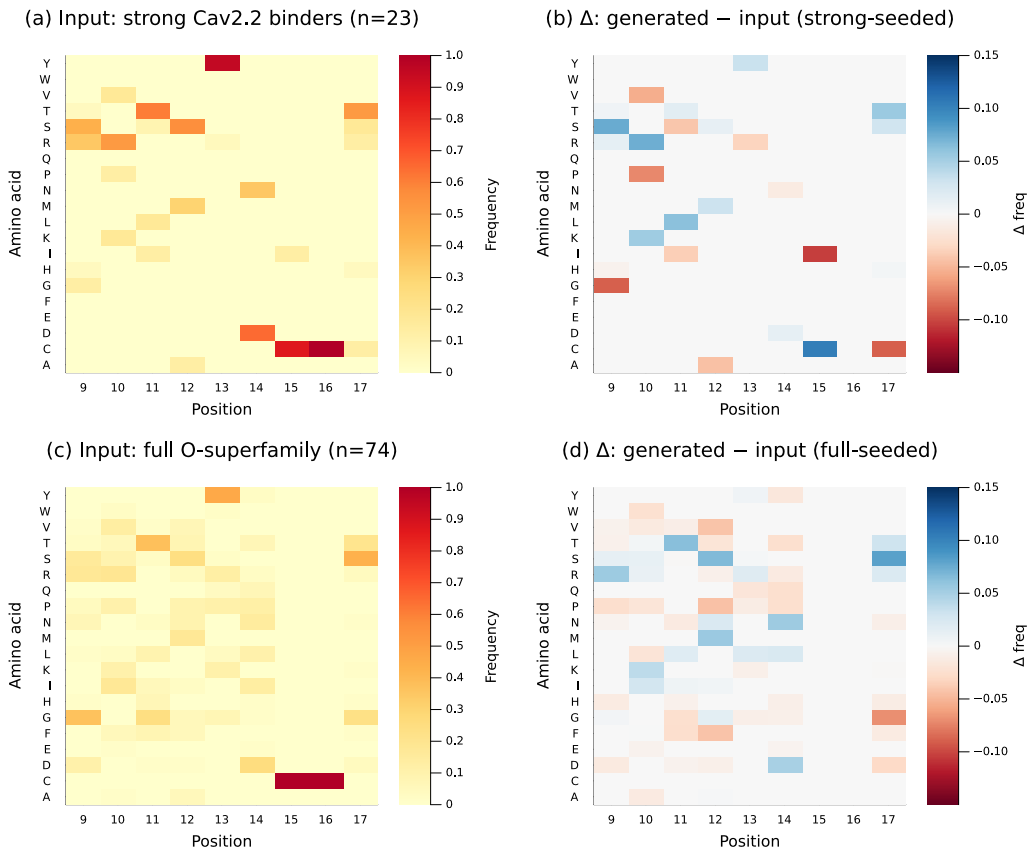
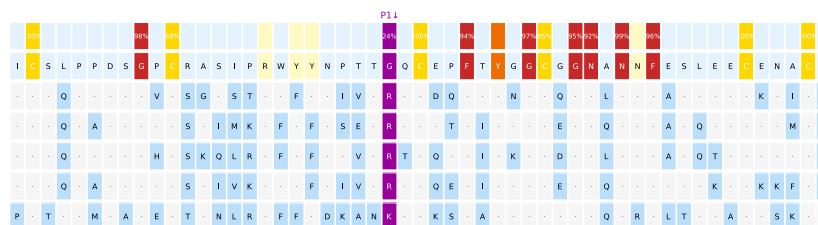


Figure 4: **Binding-loop amino acid frequencies and generation residuals for the ω -conotoxin family (positions 9–17).** *Left column:* Per-position amino acid frequency heatmaps for the input sequences (strong Cav2.2 binders, $n = 23$, panel a; full O-superfamily, $n = 74$, panel c). *Right column:* Residual heatmaps (generated – input) showing the change in frequency at each position–residue pair after SA generation. Panel (b): strong-seeded residuals are near-zero throughout ($|\Delta f| < 0.15$), confirming that the Tyr pharmacophore at position 13, the conserved Cys framework (positions 14–16), and the variable-loop diversity (positions 9–12) are reproduced with high fidelity. Panel (d): full-seeded residuals are slightly larger, reflecting the broader sequence diversity of the input. Blue: enrichment; red: depletion; white: no change.

(A) Kunitz domain: consensus vs. top SA strong-binder-conditioned sequences



(B) Per-position entropy: stored MSA vs. SA-generated sequences

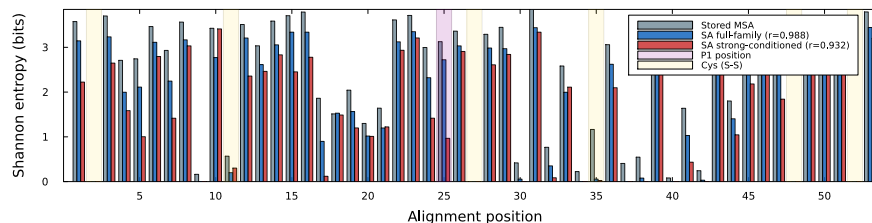
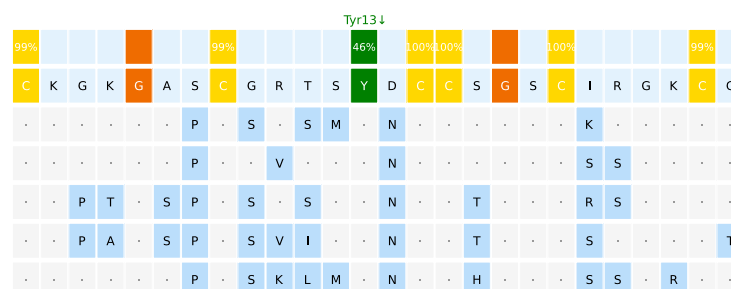


Figure 5: Sequence-level analysis of SA-generated Kunitz domain sequences conditioned on strong trypsin binders. (A) Alignment of the family consensus with the five highest-confidence SA strong-binder-conditioned sequences (ranked by ESMFold pLDDT). Positions are colored by conservation in the stored MSA: highly conserved (> 90%, red), conserved (70–90%, orange), moderate (50–70%, yellow), and variable (< 50%, blue). Cysteines forming the three disulfide bonds are highlighted in gold; the P1 position is highlighted in purple. Dots indicate matches to the consensus; letters indicate substitutions. All five sequences preserve every highly conserved position (11/11), all six cysteines (6/6), and carry K or R at P1, while introducing 19–26 substitutions concentrated at variable sites. (B) Per-position Shannon entropy for the stored MSA (gray), SA full-family generation (blue), and SA strong-binder-conditioned generation (red). The full-family entropy correlation is very high ($r = 0.988$), confirming that SA recapitulates the position-specific conservation pattern of the natural family. The strong-conditioned entropy correlation is slightly lower ($r = 0.932$), with the largest deviation at the P1 position (column 25): conditioning collapses P1 diversity to K/R, reducing entropy at this site while preserving the entropy profile elsewhere.

(A) ω -Conotoxin: consensus vs. top SA strong-binder-conditioned sequences



(B) Per-position entropy: stored MSA vs. SA-generated sequences

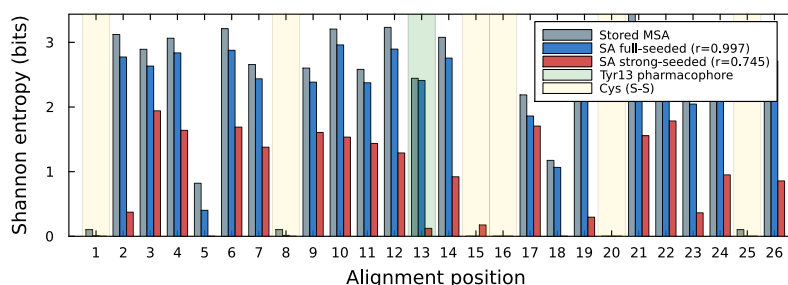


Figure 6: Sequence-level analysis of SA-generated ω -conotoxin sequences conditioned on strong Cav2.2 binders. (A) Alignment of the family consensus with the five highest-confidence SA strong-binder-conditioned sequences (ranked by ESMFold pLDDT). Positions are colored by conservation in the stored MSA: highly conserved ($> 90\%$, red), conserved ($70\text{--}90\%$, orange), moderate ($50\text{--}70\%$, yellow), and variable ($< 50\%$, blue). Cysteines forming the three disulfide bonds are highlighted in gold; the Tyr13 pharmacophore position is highlighted in green. All five sequences preserve every highly conserved position (6/6), all six cysteines (6/6), and carry Tyr at the pharmacophore position, while introducing 5–11 substitutions concentrated at variable sites. (B) Per-position Shannon entropy for the stored MSA (gray), SA full-seeded generation (blue), and SA strong-seeded generation (red). The full-seeded entropy correlation is near-perfect ($r = 0.997$), confirming faithful recapitulation of position-specific conservation. The strong-seeded correlation is lower ($r = 0.745$), reflecting the fact that conditioning on 23 strong Cav2.2 binders collapses diversity not only at the Tyr13 pharmacophore but also at co-varying loop residues that contribute to channel binding specificity.

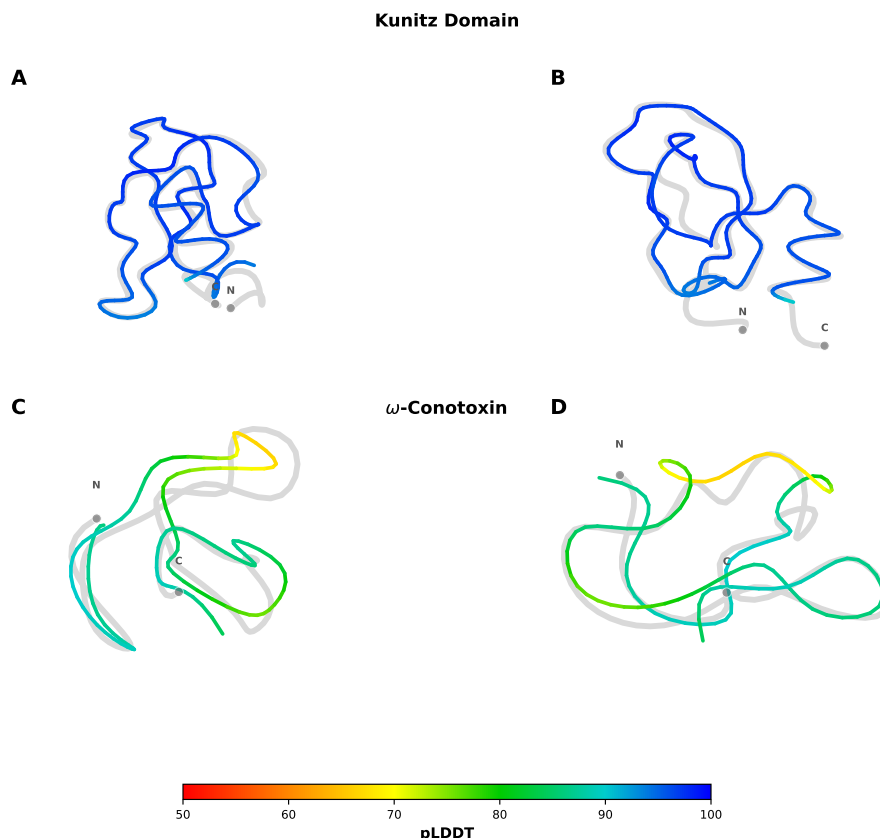


Figure 7: SA-generated sequences fold into native-like structures for both protein families. For each family, the single highest TM-score SA strong-conditioned sequence (colored by per-residue pLDDT confidence) is superimposed onto the experimental reference structure (gray, semi-transparent) and shown in two orthogonal views (front and 90° rotation) to reveal the full three-dimensional architecture. **(A)** Kunitz domain, front view. **(B)** Kunitz domain, 90° rotation. The SA-generated variant aligns to the BPTI crystal structure (1BPI chain A) with $TM = 0.94$, reproducing the double-loop architecture, three-stranded antiparallel β -sheet, and α -helical turn; pLDDT > 90 throughout (deep blue) indicates high-confidence prediction. **(C)** ω -Conotoxin, front view. **(D)** ω -Conotoxin, 90° rotation. The SA-generated variant aligns to the MVIIA NMR structure (1OMG chain A) with $TM = 0.53$, consistent with the small peptide length (26 residues) where TM-score normalization is noisy; the cystine-knot topology and loop architecture are preserved, with pLDDT ~ 80 (cyan/green) reflecting the intrinsic flexibility of the inter-cysteine loops. Colorbar: pLDDT confidence scale (red = 50, blue = 100). Structures predicted by ESMFold [5]; alignment by TM-align [20].

SI Appendix

S1 Sequence Encoding, PCA Projection, and Multiplicity Conditioning

Stochastic attention (SA) operates on continuous vectors on the unit sphere, while protein sequences are discrete objects over a 20-letter amino acid alphabet. Bridging the two requires three transformations (one-hot encoding, PCA dimensionality reduction, and unit-norm projection), and the reverse path (inverse PCA followed by argmax decoding) recovers discrete sequences from continuous samples. Here we describe the full encoding–decoding pipeline, derive the multiplicity-weighted conditioning formulas used in the main text, and discuss how the multiplicity vector \mathbf{r} interacts with the PCA representation.

Given a cleaned alignment of K sequences, each of length L amino acids over the standard 20-letter alphabet $\mathcal{A} = \{\text{A, R, N, } \dots, \text{V}\}$, we encoded each sequence as a binary vector in \mathbb{R}^{20L} by concatenating per-position indicator vectors. For sequence k ($k = 1, \dots, K$) with amino acid $a_\ell^{(k)}$ at alignment position ℓ ($\ell = 1, \dots, L$):

$$\mathbf{x}_k = [\mathbf{e}_{a_1^{(k)}}, \mathbf{e}_{a_2^{(k)}}, \dots, \mathbf{e}_{a_L^{(k)}}]^\top \in \{0, 1\}^{20L}, \quad (8)$$

where $\mathbf{e}_a \in \{0, 1\}^{20}$ is the standard basis vector for amino acid a (i.e., a one-hot indicator with a 1 in the position corresponding to a and 0 elsewhere). The full one-hot dimensionality is $d_{\text{full}} = 20L$, which ranged from 520 (ω -conotoxin, $L=26$) to 1,060 (Kunitz, $L=53$) across the four families. This space is over-dimensioned relative to the number of stored patterns K (d_{full}/K ranged from 7.0 to 10.7), which creates a problem for the modern Hopfield energy [19]: the similarity score $e_k = \mathbf{m}_k^\top \boldsymbol{\xi}$ between a stored pattern \mathbf{m}_k and a query state $\boldsymbol{\xi}$ has variance $1/d$ for a random query on the unit sphere \mathbb{S}^{d-1} , so when d is large all scores concentrate near zero and the inverse temperature β must be set extremely high to differentiate among patterns, making Langevin sampling inefficient. PCA removes this redundancy by projecting onto the $d \ll d_{\text{full}}$ directions of actual variation in the alignment.

We computed PCA from the one-hot encoded alignment by first centering the data: $\bar{\mathbf{x}} = K^{-1} \sum_{k=1}^K \mathbf{x}_k$ (the family’s position-specific amino acid frequency profile), $\tilde{\mathbf{X}} = \mathbf{X} - \bar{\mathbf{x}} \mathbf{1}_K^\top$, and then computing the economy SVD $\tilde{\mathbf{X}} = \mathbf{U} \boldsymbol{\Sigma} \mathbf{V}^\top$, where $\mathbf{U} \in \mathbb{R}^{d_{\text{full}} \times r}$ contains the principal directions of variation, $\boldsymbol{\Sigma} = \text{diag}(\sigma_1, \dots, \sigma_r)$ the singular values in decreasing order, and $r = \text{rank}(\tilde{\mathbf{X}}) \leq \min(d_{\text{full}}, K) - 1$. We retained the smallest dimension d such that $\sum_{j=1}^d \sigma_j^2 / \sum_{j=1}^r \sigma_j^2 \geq 0.95$ (at least 95% of total variance). Across the four families, d ranged from 34 (ω -conotoxin) to 186 (WW), yielding compression ratios of $3.3\times$ to $21\times$ (Table 1). Each sequence was then projected as $\mathbf{z}_k = \mathbf{W}_d^\top (\mathbf{x}_k - \bar{\mathbf{x}}) \in \mathbb{R}^d$, where $\mathbf{W}_d = \mathbf{U}_{:,1:d}$ is the projection matrix, and normalized to unit L_2 norm: $\mathbf{m}_k = \mathbf{z}_k / \|\mathbf{z}_k\|_2 \in \mathbb{S}^{d-1}$. This normalization ensures that similarity scores lie in $[-1, 1]$ and prevents patterns with larger PCA norms from dominating the softmax attention. The columns $\mathbf{m}_1, \dots, \mathbf{m}_K$ form the memory matrix $\hat{\mathbf{X}} \in \mathbb{R}^{d \times K}$ used throughout the paper. The Langevin sampler (Eq. 1) produces continuous states $\boldsymbol{\xi} \in \mathbb{R}^d$, which are decoded back to amino acid sequences by inverse PCA reconstruction $\hat{\mathbf{x}} = \bar{\mathbf{x}} + \mathbf{W}_d \boldsymbol{\xi} \in \mathbb{R}^{d_{\text{full}}}$ followed by per-position argmax: $a_\ell = \arg \max_{a \in \mathcal{A}} \hat{x}_{20(\ell-1)+a}$ for $\ell = 1, \dots, L$. This decoding is deterministic and produced valid amino acids at 100% of positions across all families and conditions.

The multiplicity-weighted Hopfield energy (Eq. 2) assigns a weight $r_k > 0$ to each stored pattern \mathbf{m}_k . For the binary functional split used throughout this paper, we set $r_k = \rho$ for the K_{des} designated patterns and $r_k = 1$ for the $K_{\text{bg}} = K - K_{\text{des}}$ background patterns, where $\rho \geq 1$ is the multiplicity ratio. The weighted score function (Proposition 1) adds $\log \rho$ to the pre-softmax logits of designated patterns and $\log 1 = 0$ to background patterns. To derive the effect of ρ on the attention distribution, consider the idealized case where the query $\boldsymbol{\xi}$ has equal similarity to all stored patterns, i.e., $\mathbf{m}_k^\top \boldsymbol{\xi} = c$ for all k . The softmax attention weight on pattern k simplifies to $a_k = r_k / \sum_j r_j$, and the total attention weight on all designated patterns is:

$$f_{\text{eff}}(\rho) = \sum_{k \in \text{des}} a_k = \frac{K_{\text{des}} \rho}{K_{\text{des}} \rho + K_{\text{bg}}}. \quad (9)$$

At $\rho = 1$, $f_{\text{eff}} = K_{\text{des}}/K$ (the natural proportion); as $\rho \rightarrow \infty$, $f_{\text{eff}} \rightarrow 1$. To find the multiplicity ratio needed for a target effective fraction $f \in (0, 1)$, we invert Eq. (9) by multiplying both sides by

the denominator and solving for ρ :

$$\begin{aligned}
 f(K_{\text{des}}\rho + K_{\text{bg}}) &= K_{\text{des}}\rho, \\
 fK_{\text{bg}} &= K_{\text{des}}\rho(1-f), \\
 \rho(f) &= \frac{fK_{\text{bg}}}{K_{\text{des}}(1-f)}.
 \end{aligned}
 \tag{10}$$

This is Eq. (4) in the main text. The formula is exact under the equal-similarity assumption; in practice, we confirmed empirically that the mean attention weight on designated patterns tracked $f_{\text{eff}}(\rho)$ with $< 0.3\%$ deviation across all ρ values and all families (Table 2), validating the approximation as operationally exact. The effective number of patterns under multiplicity weighting, $K_{\text{eff}}(\mathbf{r}) = (\sum_k r_k)^2 / \sum_k r_k^2 = (K_{\text{des}}\rho + K_{\text{bg}})^2 / (K_{\text{des}}\rho^2 + K_{\text{bg}})$, equals K when $\rho = 1$ and converges to K_{des} as $\rho \rightarrow \infty$; this quantity governs the shift in the phase transition temperature β^* .

A key property of multiplicity-weighted conditioning is that \mathbf{r} does *not* alter the PCA encoding. The memory matrix $\tilde{\mathbf{X}}$ is constructed once from the full family alignment and remains fixed regardless of ρ ; the multiplicity weights enter only through the softmax logits. This separation has three consequences. First, the PCA subspace is independent of ρ : the principal directions \mathbf{W}_d , the centering vector $\tilde{\mathbf{x}}$, and the retained dimension d are all determined by the alignment alone, so the calibration gap $\Delta = f_{\text{eff}} - f_{\text{obs}}$ is identical for all ρ values on a given family. Second, ρ controls attention, not geometry: increasing ρ adds $\log \rho$ to the designated logits, shifting attention weight toward designated patterns, but this shift must still pass through the PCA reconstruction and argmax decoding to produce discrete residues, which is where the calibration gap arises. Third, ρ shifts the phase transition: the logit biases pre-concentrate the attention distribution at $\beta = 0$, reducing the weighted entropy to $H_{\mathbf{r}}(0) = \log K_{\text{eff}}(\mathbf{r}) < \log K$, so reaching the retrieval-phase inflection requires a higher inverse temperature $\beta^*(\rho) \geq \beta^*(1)$. We observed this empirically: β^* increased from 4.4 ($\rho = 1, K_{\text{eff}} = 99$) to 9.3 ($\rho = 1,000, K_{\text{eff}} = 32.1$) on the Kunitz domain (Fig. 2). By contrast, hard curation (where the memory matrix is built from the designated subset only) *does* change the PCA: the centering vector, principal directions, and retained dimension are all computed from K_{des} sequences, capturing subset-specific variation that may be orthogonal to the leading components of the full-family PCA. This is why hard curation achieved 100% phenotype transfer regardless of the Fisher separation index S , while multiplicity weighting was limited by the full-family PCA geometry.

S2 Supplementary Tables and Figures

Tables S1–S5 report selected values from the ρ sweep on each of the five Pfam benchmark families. f_{eff} is the effective designated fraction computed from the multiplicity vector; f_{obs} is the hard-decoded marker fraction averaged over 930 generated sequences; \bar{a}_{des} is the mean softmax attention weight on designated patterns; and D is the mean pairwise diversity. Table S6 reports phenotype fraction and diversity as a function of β/β^* for three fixed ρ values on the Kunitz domain. Figure S1 shows the joint distribution of ESMFold pLDDT and TM-score for all 250 predicted Kunitz structures: SA-generated sequences cluster tightly in the high-pLDDT, high-TM-score region while HMM-emitted sequences scatter broadly across lower values. The entropy curves for the full ρ sweep ($\rho \in \{1, 2, 5, 10, 20, 50, 100, 200, 500, 1000\}$) on the Kunitz family produce a monotonically rightward-shifting family of sigmoid curves with $\beta^*(\rho)$ increasing from 4.35 ($\rho = 1$) to 9.26 ($\rho = 1000$), consistent with $\beta^* \propto \log K_{\text{eff}}$ predicted by the mean-field argument in Section 4.1 (Fig. 2).

Table S1: Kunitz domain (PF00014) ρ sweep. $K = 99, K_{\text{des}} = 32$.

ρ	f_{eff}	f_{obs}	\bar{a}_{des}	D
1	0.323	0.406	0.324	0.563
5	0.705	0.481	0.712	0.556
10	0.827	0.539	0.832	0.547
50	0.962	0.598	0.963	0.526
100	0.980	0.615	0.981	0.520
200	0.990	0.623	0.991	0.519
500	0.996	0.631	0.997	0.515
1000	0.998	0.634	0.998	0.514

Table S2: SH3 domain (PF00018) ρ sweep. $K = 55$, $K_{\text{des}} = 33$.

ρ	f_{eff}	f_{obs}	\bar{a}_{des}	D
1	0.600	0.852	0.614	0.580
5	0.882	0.897	0.890	0.575
10	0.938	0.906	0.941	0.575
50	0.983	0.965	0.983	0.567
100	0.991	0.977	0.991	0.559
200	0.996	0.984	0.996	0.554
500	0.999	0.989	0.999	0.513
1000	0.999	0.992	0.999	0.510

Docking-statistics note

For the ω -conotoxin docking validation (Table 7), group-level comparisons (SA strong-conditioned, SA full-conditioned, and natural ω -conotoxin controls) were evaluated using exact two-sided permutation tests on mean complex-level scores (iPTM, pTM, confidence, and interface-pLDDT), with sample sizes $n_{\text{SA, strong}} = 10$, $n_{\text{SA, full}} = 10$, and $n_{\text{control}} = 5$. No pairwise contrast reached significance at $\alpha = 0.05$ (all $p > 0.05$; smallest observed $p = 0.0726$ for confidence, SA full vs controls).

Table S3: WW domain (PF00397) ρ sweep. $K = 420$, $K_{\text{des}} = 69$.

ρ	f_{eff}	f_{obs}	\bar{a}_{des}	D
1	0.164	0.131	0.152	0.690
5	0.496	0.184	0.487	0.689
10	0.663	0.226	0.661	0.676
50	0.901	0.277	0.901	0.657
100	0.947	0.303	0.947	0.649
200	0.973	0.327	0.974	0.643
500	0.990	0.360	0.991	0.642
1000	0.995	0.371	0.995	0.642

Table S4: Homeobox domain (PF00046) ρ sweep. $K = 136$, $K_{\text{des}} = 102$.

ρ	f_{eff}	f_{obs}	\bar{a}_{des}	D
1	0.750	0.935	0.758	0.525
5	0.938	0.954	0.939	0.521
10	0.968	0.955	0.969	0.522
50	0.993	0.957	0.994	0.521
100	0.997	0.957	0.997	0.521
200	0.998	0.957	0.998	0.521
500	0.999	0.957	0.999	0.521
1000	1.000	0.957	1.000	0.521

Table S5: Forkhead domain (PF00250) ρ sweep. $K = 246$, $K_{\text{des}} = 122$.

ρ	f_{eff}	f_{obs}	\bar{a}_{des}	D
1	0.496	0.556	0.490	0.480
5	0.831	0.610	0.826	0.464
10	0.908	0.638	0.904	0.447
50	0.980	0.670	0.979	0.431
100	0.990	0.710	0.988	0.417
200	0.995	0.711	0.994	0.416
500	0.998	0.730	0.998	0.399
1000	0.999	0.730	0.999	0.398

Table S6: β sweep on Kunitz domain ($K = 99$, $K_{\text{des}} = 32$).

ρ	β/β^*	f_{obs}	D
10	0.50	0.471	0.581
10	1.00	0.539	0.547
10	1.50	0.573	0.525
10	2.00	0.597	0.508
10	3.00	0.613	0.484
50	0.50	0.506	0.573
50	1.00	0.582	0.537
50	1.50	0.631	0.514
50	2.00	0.653	0.499
50	3.00	0.700	0.469
200	0.50	0.535	0.564
200	1.00	0.613	0.527
200	1.50	0.648	0.503
200	2.00	0.677	0.488
200	3.00	0.706	0.463

Table S7: Pairwise exact permutation p-values for ω -conotoxin docking comparisons (all H_0 : equal means).

Metric	SA strong vs SA full	SA strong vs controls	SA full vs controls
iPTM	1.0000	0.7502	0.4752
pTM	0.7873	0.1285	0.1092
Confidence	0.6560	0.1245	0.0726
Interface pLDDT	0.6556	0.2238	0.2934

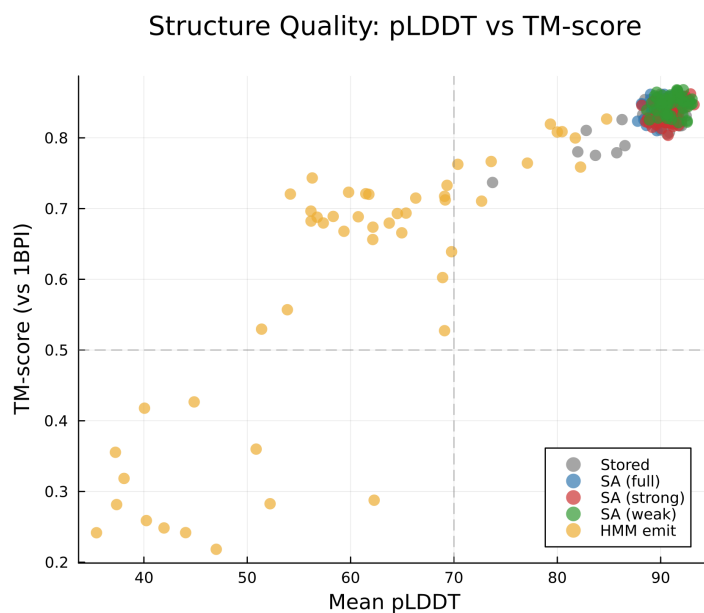


Figure S1: **pLDDT and TM-score are positively correlated; SA sequences cluster in the high-quality region.** Each point represents one predicted structure (50 per source). Stored (gray) and SA-generated (blue, red, green) sequences cluster tightly above pLDDT > 85 and TM-score > 0.8 (upper right quadrant). HMM sequences (orange) scatter broadly, with many falling below the pLDDT > 70 confidence threshold (vertical dashed line) and the TM-score > 0.5 same-fold threshold (horizontal dashed line).